fractal and fractional

MDPI

Article

Application of an Optimal Fractional-Order Controller for a Standalone (Wind/Photovoltaic) Microgrid Utilizing Hybrid Storage (Battery/Ultracapacitor) System

Hani Albalawi [1,2], Sherif A. Zaid [1,*], Aadel M. Alatwi [1,3] and Mohamed Ahmed Moustafa [4]

[1] Electrical Engineering Department, Faculty of Engineering, University of Tabuk, Tabuk 47913, Saudi Arabia; halbala@ut.edu.sa (H.A.); adalatawi@ut.edu.sa (A.M.A.)
[2] Renewable Energy and Environmental Technology Centre, University of Tabuk, Tabuk 47913, Saudi Arabia
[3] Industrial Innovation and Robotic Center (IIRC), University of Tabuk, Tabuk 47731, Saudi Arabia
[4] Department of Electrical Power, Faculty of Engineering, Cairo University, Giza 82524, Egypt; mmustafa@eng.cu.edu.eg
* Correspondence: shfaraj@ut.edu.sa

Abstract: Nowadays, standalone microgrids that make use of renewable energy sources have gained great interest. They provide a viable solution for rural electrification and decrease the burden on the utility grid. However, because standalone microgrids are nonlinear and time-varying, controlling and managing their energy can be difficult. A fractional-order proportional integral (FOPI) controller was proposed in this study to enhance a standalone microgrid's energy management and performance. An ultra-capacitor (UC) and a battery, called a hybrid energy storage scheme, were employed as the microgrid's energy storage system. The microgrid was primarily powered by solar and wind power. To achieve optimal performance, the FOPI's parameters were ideally generated using the gorilla troop optimization (GTO) technique. The FOPI controller's performance was contrasted with a conventional PI controller in terms of variations in load power, wind speed, and solar insolation. The microgrid was modeled and simulated using MATLAB/Simulink software R2023a 23.1. The results indicate that, in comparison to the traditional PI controller, the proposed FOPI controller significantly improved the microgrid's transient performance. The load voltage and frequency were maintained constant against the least amount of disturbance despite variations in wind speed, photovoltaic intensity, and load power. In contrast, the storage battery precisely stores and releases energy to counteract variations in wind and photovoltaic power. The outcomes validate that in the presence of the UC, the microgrid performance is improved. However, the improvement is very close to that gained when using the proposed controller without UC. Hence, the proposed controller can reduce the cost, weight, and space of the system. Moreover, a Hardware-in-the-Loop (HIL) emulator was implemented using a C2000™ microcontroller LaunchPad™ TMS320F28379D kit (Texas Instruments, Dallas, TX, USA) to evaluate the proposed system and validate the simulation results.

Keywords: wind energy; photovoltaic (PV); ultra-capacitor (UC); fractional-order proportional integral (FOPI); gorilla troop optimization (GTO)

Citation: Albalawi, H.; Zaid, S.A.; Alatwi, A.M.; Moustafa, M.A. Application of an Optimal Fractional-Order Controller for a Standalone (Wind/Photovoltaic) Microgrid Utilizing Hybrid Storage (Battery/Ultracapacitor) System. *Fractal Fract.* **2024**, *8*, 629. https://doi.org/10.3390/fractalfract8110629

Academic Editors: Arman Oshnoei and Mahdieh S. Sadabadi

Received: 15 September 2024
Revised: 22 October 2024
Accepted: 22 October 2024
Published: 25 October 2024

Correction Statement: This article has been republished with a minor change. The change does not affect the scientific content of the article and further details are available within the backmatter of the website version of this article.

1. Introduction

An increasing population and global industrial development coincided with the start of this century. This led to a rise in global electricity demand. But conventional electricity sources have numerous environmental issues and are insufficient [1–4]. As a result, attention has been drawn to renewable electricity sources (wind, solar, tidal, etc.). The environmental benefits of renewable electricity resources are numerous. However, a common drawback of them is their sporadic nature [5]. When a system is linked to a major utility grid, an intermittent energy supply might not be a significant issue. Small microgrids and isolated systems will be particularly affected by this issue, though. Hybrid

energy systems, which integrate two or more renewable resources, are one approach to address the intermittency issue [6]. A wind/PV hybrid is a typical example of this kind of microgrid [7].

Even though solar and wind energy sources fluctuate, they could work together to help mitigate the issue of intermittency. In the day, solar energy is available. There is no set time of day when wind energy is most accessible. On the other hand, there are some situations where nighttime wind energy exceeds daytime wind energy. As a result, the two energy resources are integrated in some way. As a result, hybrid PV/wind systems are regarded as dependable and practical substitutes for battery-based wind and solar diesel systems in standalone applications [8].

For hybrid wind/photovoltaic systems, several research publications have been selected [5,6,9–15]. Reference [9] suggests that the boost converter in a traditional wind/photovoltaic power system be swapped out for a PWM rectifier. For rural electrification applications, a composite sliding mode controller for load inverters was also implemented. According to reference [10], a PID technique can be employed by a dual input buck-boost converter to control the bus voltage that charges the battery from the solar module and wind turbine generator. The propulsion system of a ship model has been powered by batteries. According to this study, a PID control system may produce effective performance from wind and solar turbine generators. Reference [11] has proposed the use of an enhanced decomposition multi-objective evolutionary algorithm for the scaling of hybrid PV/battery/wind/diesel microgrids. The analysis has taken into account several factors such as parameter uncertainty, battery deterioration, viability of energy infrastructure, internal rate of return, payback time evaluation, and total expenses. There has been a study conducted on a wind farm, photovoltaic plant, concentrated solar power plant, electric heater, inverter, and battery model [12]. A wind/photovoltaic microgrid with a distributed DC bus has been proposed in Ref. [13]. The PV array's and the wind turbine's MPPT have been put into practice by the control system. The response of the power system was tested by applying step changes in the nonlinear load. A wind/photovoltaic microgrid that functioned in both AC and DC modes was presented by [14]. The control scheme was adjusted to the AC/DC microgrid power exchange. The microgrid powered both household and dynamic loads. The ideal system architecture and design considerations were determined using a variety of levelized cost of energy methodologies.

Consumption of solar and wind power is increasing as a result of our growing desire to lessen our environmental impact. In order to mitigate an unpredictable power supply, Reference [15] proposes a hybrid system that combines wind and solar generators. PV arrays, wind turbines, batteries, a standby diesel generator, converters, and other equipment are all parts of PV, battery, wind, and diesel hybrid systems. These parts produce, store, and control electricity. The primary source of the world's environmental degradation is conventional fossil fuel-based electricity generation, and this situation is only going to get worse soon.

Proportion integral derivative (PID) controllers have historically been used to operate freestanding microgrids. PID controllers are renowned for their simplicity and dependability, but they can also have drawbacks when dealing with complicated and uncertain systems, such as overshoot [16]. A recent development in control techniques, fractional-order control (FOC) is a step up from conventional integer-order control techniques and is employed in a variety of renewable energy systems. The key advantages of FOPI controllers over PI controllers are their greater flexibility due to non-integer orders; their enhanced robustness in uncertain or time-varying systems; their better frequency-domain performance, especially in low-frequency dynamics; and their improved performance in complex, non-linear, or multi-variable systems. Despite these advantages, the use of FOPI controllers may be limited by their increased computational demands and complexity of design, making them more suitable for advanced or high-performance control systems [17].

Nonlinear systems are difficult to control due to varying behavior under different conditions, making it challenging for traditional controllers to maintain stability. Fractional-

order controllers (FOCs) address this by providing additional tuning parameters (fractional orders), offering greater flexibility and improved robustness against nonlinearities like saturation and friction. This smooth transition between linear and nonlinear systems enhances performance in complex systems, such as power electronics [18]. Designing FOCs involves mathematical modeling, optimization, and discretization for digital implementation. A common approach is extending traditional PID controllers to fractional-order PID (FOPID) controllers, where both integral and derivative terms are non-integer. Tuning methods include frequency response, optimization-based techniques, and modified Ziegler–Nichols rules. For digital control, fractional derivatives and integrals are approximated using numerical methods like Grünwald–Letnikov and Oustaloup's approximation to enable real-time implementation [17].

FOC has been applied in a number of microgrids that are fed by renewable energy sources [19–22]. In order to improve the efficiency of the electrical power system, a FOPID controller based on the real-world application of automatic control techniques was used in [19] to optimize the hydraulic turbines' isochronous speed regulator. A fractional order fuzzy-PID controller was employed in [20] to manage the frequency of a hybrid system comprising a tidal and diesel power plant. The applicability of fractional order intelligent control for distributed energy generation or hybrid power systems was examined in [21]. Using various particle swarm optimization (PSO) variants, robust optimization techniques were used to tune the FOC controller parameters, which were then compared with the corresponding optimal solutions using simulation results. In [22], a new intelligent FOC controller was proposed for frequency regulation of two area interconnected energy systems. The research idea utilized the virtual inertia principle with the help of the proposed intelligent FOC controller to regulate the system voltage and frequency.

To maintain the stability and dependability of the power system, wind power's intermittent nature requires the use of energy storage devices to offset variations in wind/photovoltaic systems [23]. Additionally, these storage devices strengthen the system's ability to withstand abrupt changes in wind and load [24]. Batteries, flywheels, superconducting magnetic energy storage, ultracapacitors, thermal, compressed air storage, hydrogen, and other devices have all been used as energy storage systems. Nevertheless, because of their low cost, broad temperature range, and high cell voltage, batteries are frequently utilized in a variety of applications [25]. When compared to a single energy storage technology, the implementation of hybrid energy storage system (HESS) minimizes the initial cost because the secondary storage system just needs to meet the average power demand because power and energy are decoupled. Additionally, it increases the plant lifetime and storage capacity while improving the overall system efficiency (minimizes the dynamic stress of the secondary storage system and optimizes the operation). A UC-battery HESS was initially investigated in the literature as a potential replacement for conventional battery systems in digital communication applications that experienced pulsed loads [26]. Due to the frequent motor starts and braking events of electric vehicles, this technology is currently widely used in these vehicles. It is possible to decrease the size and extend the battery life by including a supercapacitor [27]. Due to the superior dependability and extended battery life that these battery–supercapacitor combinations produce, HESS is also being investigated for stand-alone renewable energy applications [28].

This paper describes how to manage and operate an autonomous microgrid that is powered by solar and wind energy using a FOPI controller. In addition, the microgrid uses a semiactive UC-battery HESS for energy storage. Optimal fractional-order controllers form the foundation of the proposed microgrid's energy management and control system. The primary goals of the system are to regulate the DC bus voltage, manage the energy of the system, and operate the semiactive UC-battery HES. Using the GTO optimization technique, the fractional-order controller's gains were optimally selected. Additionally, evaluations of the proposed FOPI controller's performance in comparison to the conventional PI controller were conducted. Additionally, a comparison was made between the proposed microgrid's performance with and without the UC, utilizing the optimized

FOPI controller. The MATLAB/Simulink platform was utilized to model and simulate the proposed wind/photovoltaic microgrid. The goals of this study were as follows:

- FOPI controllers were incorporated to improve the recommended microgrid's functionality.
- The metaheuristic optimization method known as GTO was utilized to ascertain the optimal parameters of the proposed FOPI controller.
- The effectiveness of the proposed microgrid with and without the UC was assessed utilizing the FOPI controller.
- A comparison was made between the performance of the proposed system with the FOPI controller and the traditional PI. The controller's performance was assessed in a range of load power, solar, and wind energy disturbances.
- The proposed system was modeled in MATLAB. The system's performance was assessed to find out how variations in wind and solar energy affected the microgrid's response.

This manuscript is organized as follows: Section 2 provides a summary of the proposed microgrid; Section 3 describes the hybrid energy storage configurations; Section 4 presents the proposed control structure; Section 5 covers the simulation results; and Section 6 presents the conclusions.

2. The Examined Microgrid's Overview

Figure 1 shows the planned autonomous microgrid powered by solar PV and wind energy resources. In the day, solar energy is available, however, it is not available at night. There is no set time of day when wind energy is most accessible. On the other hand, there are some situations where nighttime wind energy exceeds daytime wind energy. As a result, the two energy resources are integrated in some way. Nevertheless, because of the fluctuations in the weather and solar radiation, they are unable to produce consistent energy. The intermittent nature of solar and wind energy is caused by these problems. As a result, using both resources improves the microgrid's sustainability and dependability. Additionally, the energy storage system's dimensions will be lowered.

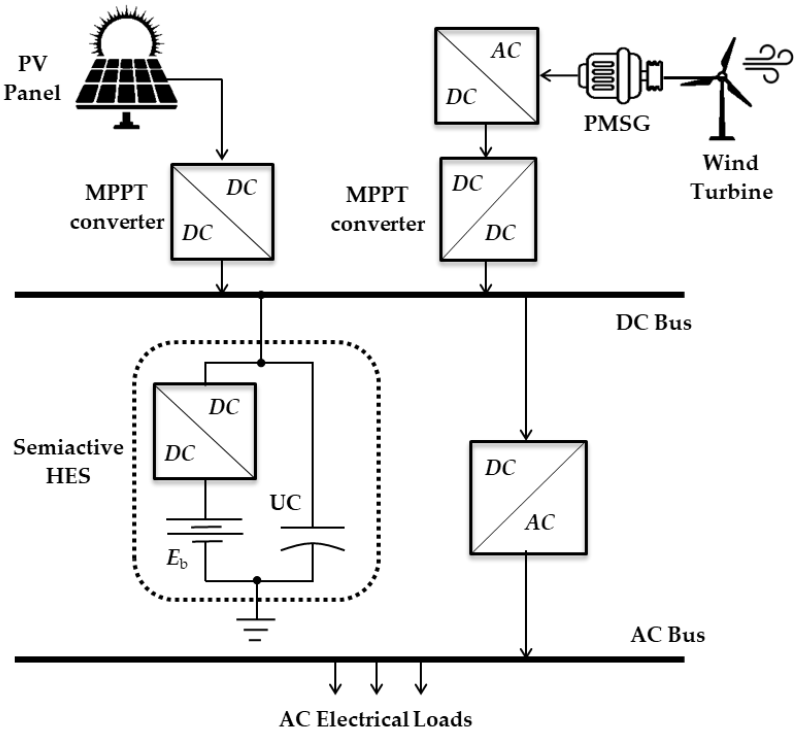

Figure 1. The power circuit topology of the proposed microgrid.

The wind system consists of a 3 − φ permanent magnet synchronous generator mechanically linked to a wind turbine. An uncontrolled rectifier is used to rectify the generator output, producing an unregulated DC voltage. A boost converter is powered by this voltage. The wind turbine is pushed toward the MPPT conditions by the boost converter. The microgrid's DC bus is connected to the boost converter's output. Three parallel strings make up the PV array that powers the solar energy system. Modules are included in every string. This PV output is fed into an additional boost converter. Additionally, the PV's MPPT conditions are implemented via the boost converter.

As a result of the generated energy's intermittent nature, HESS is used to offset the energy intermittency issue and maintain system stability. Besides a UC, a series-parallel arrangement of lead–acid batteries makes up the HES. A bidirectional DC/DC converter connects the batteries to the DC bus. On the other hand, the UC is directly connected to the DC bus. Semi-active HESS is the name given to this topology of the HESS. Its job is to control how the energy storage system is discharged and charged. Furthermore, that converter serves as the primary actuator for microgrid energy balance and DC bus voltage adjustments.

3. Hybrid Energy Storage Configurations

Energy storage technologies can be classified as high power and high energy storage systems (HPS and HES) [29]. Each energy storage technology has its own restrictions, which limit the variety of applications that it may be used for. This is because the ideal operation requires the integration of high power and high energy storage elements. In order to create a HESS, a system that mixes two or more energy storage equipment types must be built [30]. Batteries, for instance, have low specific power, high specific energy, a shorter life cycle, a lower self-discharge capacity, and a lower cost per watt-hour. However, a UC has a higher self-discharge, a longer lifespan, faster charging, less specific energy, and greater specific power [31]. Consequently, a battery–UC mixture can make use of each other's complementing characteristics. This combination's symmetrical functioning concept, wide availability, and inexpensive initial cost have made it popular.

Generally, the two-energy storage elements in a battery–UC HESS can be connected to a common AC or DC bus [32]. A common DC bus is the recommended option for freestanding microgrids for several reasons [33]. First off, DC voltage is used by most energy storage system components and renewable energy sources. Consequently, keeping a DC bus minimizes the requirement for a power converter [34]. Second, DC buses do not need to be synchronized, which significantly lowers the system's overall complexity [35]. Consequently, DC coupling is less expensive and more efficient than comparable AC bus systems [36].

In forming a battery–UC circuit for DC bus systems, the battery and UC may be connected by three common topologies, namely, passive, semi-active, and active. Figure 2 illustrates the typical topologies for a battery–UC HESS. The subsequent subsections will provide a description and an explanation of each topology.

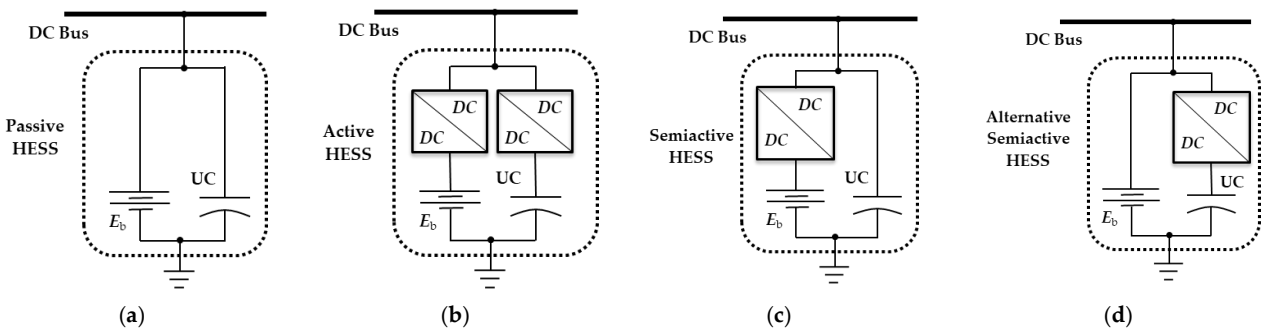

Figure 2. The typical topologies for a battery–UC HESS. (**a**) Passive topology, (**b**) active topology, (**c**) semi-active topology, and (**d**) alternative semi-active topology.

3.1. Passive HESS Topology

The straightforward method of linking a HPS and HES to a system shown in Figure 2a is known as passive architecture. Without the need for power converters, the energy storage systems are connected directly to one another [37]. The passive topology is like synchronous generators that operate in parallel and share the load according to the impedance ratio. In a similar vein, the ESS's internal resistance and output parameters determine how the load is divided. where the state of charge and the temperature have a major impact on the resistance. For example, in a battery–UC hybrid, the low impedance of the UC absorbs the high-power pulses. Hence, the UC acts as a low pass filter for power variations.

Equation (1) provides the system's power balance, where Pg, Ps, and Pl stand for power produced, power transferred by HESS, and power used by the load, in that order. The total power supplied by HPS and HES, as indicated by the second portion of (1), is the power exchanged by HESS.

$$P_s = \begin{cases} P_g - P_l \\ P_{HPS} + P_{HES} \end{cases} \quad (1)$$

This architecture was first applied to battery–UC hybrid vehicles and pulse loads. Later, it was utilized for power system applications [29,38]. In isolated microgrids, battery–UC with passive connectivity has recently been employed to reduce the intermittency of RES [26]. Nevertheless, the following drawbacks prevented this topology from receiving much interest: lack of power control flexibility that is dependent on the internal resistance; because energy storage systems are directly connected to the power system, they are susceptible to progressive setback in dangers; and the DC link or load voltage and the energy storage voltage must match precisely.

3.2. Active HESS Topology

To regulate HPS and HES, the active architecture uses a split bidirectional DC–DC converter (see Figure 2b). With the two energy storage items being independently controlled, this design provides the maximum level of controllability. It makes it easier to use the complementing qualities of HPS and HES in the energy management plan. Moreover, it facilitates the implementation of an extensive range of control methodologies. All of these benefits, nevertheless, come at the price of higher power conversion losses and higher converter costs.

$$P_s = \mu P_{HPS} + \alpha P_{HES} \quad (2)$$

Equation (2) gives the power transferred by HESS with this topology. The controllability of HPS and HES are represented by the variables μ and α, respectively. These variables are determined by the control techniques using a number of criteria, including SOC, power variation frequency, and battery deterioration rate. This architecture has been applied to HESS in power systems significantly more frequently than any other. There are two categories for this: series active topology and parallel active topology. In order to interface HPS and HES in parallel, the parallel topology uses two different sets of converters. In contrast, the series topology decouples the HPS and HES from the DC bus by cascading them with a power converter [39–41]. Because the power converter must be rated to the HESS's overall power rating, the series topology is frequently disregarded. Thus, power system applications have made extensive use of parallel active topology. This architecture has a number of benefits, including: more flexibility due to separate control of the HPS and HES; numerous different control techniques are available for use; the system voltage has no bearing on the voltage levels of the energy storage system; with converters that separate the energy storage system from the system, it has built-in fault tolerance.

3.3. Semi-Active HESS Topology

Using a single power converter to operate HPS, this topology is an expansion of the passive topology, where an appropriate control algorithm and a bidirectional DC–DC converter are utilized to manage the power exchanged by HPS (refer to Figure 2c). Equation

(3) provides the power exchanged by HESS with this topology, where β indicates HPS controllability and establishes the HPS power share. HPS meets the system's peak power requirements, while HES handles the remainder demand. Semi-active topologies with controlled batteries and controlled UC have been examined in a study. The UC power converter is too big to manage the output power of the pulse. On the other hand, the DC link voltage varies in the topology with a regulated battery [42].

$$P_s = \mu P_{HPS} + P_{HES} \quad (3)$$

Consequently, anytime a HES is interfaced with a converter, significantly large energy storage is required to maintain the DC bus voltage. Lately, a wind-supplied remote microgrid has been supported by a hybrid battery–SMES system. Because the SMES can absorb high frequency power changes, it has been utilized to increase battery longevity. Likewise, the variations of small wind-supplied systems have been suppressed with the use of a battery–UC hybrid. Another semiactive HESS design is depicted in Figure 2d, where the battery is linked directly to the DC bus and only the UC is interfaced to the DC bus via a bidirectional DC/DC converter [43]. The bidirectional DC/DC converter in this design separates the battery terminal and DC bus from the supercapacitor. The volumetric efficiency of the supercapacitor is much increased in this configuration since it may be operated over a greater voltage range. A stable DC bus voltage is also guaranteed by the battery's direct connection [33]. Despite providing some flexibility, it has the following drawback: when an HPS is interfaced directly with the system, the DC bus and voltage fluctuates; the DC–DC converter must be built to withstand the significant power spikes. Consequently, the battery's longevity is negatively impacted by the battery's inevitable exposure to significant current fluctuations due to the passive connection [42]. Many control techniques have been adapted for this topology. The control techniques can be classified as classical and intelligent techniques. The classical techniques include filtration based, rule based, dead beat, and droop controllers [29]. On the other hand, many intelligent control techniques have been adapted for HESS such as: model predictive control; fuzzy logic control; and robust control [29].

4. The Proposed Control Framework

The wind/PV MPPT controllers, the semiactive HESS controller, and the load inverter controller are the proposed system controllers depicted in Figure 3. The MPPT controllers' duties include obtaining the maximum power output from the PV array and wind turbine. They produce the necessary duty cycle signal for the boost converter, which loads the PV array and wind turbine under MPPT load circumstances. On the other hand, the HESS's charge/discharge process and the DC link voltage are regulated by the semiactive HESS controller. The frequency and voltage of the load inverter are controlled by the third controller. The descriptions of these controllers are as follows:

4.1. The Wind and PV's MPPT Controllers

For optimal wind and photovoltaic energy consumption, these controllers are essential. The popular and widely used MPPT technique known as perturb and observe has been implemented here for both controllers, as Figure 3a indicates. It offers the advantages of an easy algorithm and simple implementation. For this problem, two boost converters are used: one for the PV panel and one for the wind. The duty cycle switch value of the boost converter is the output of every MPPT controller. For both energy sources, the algorithm is the same [44].

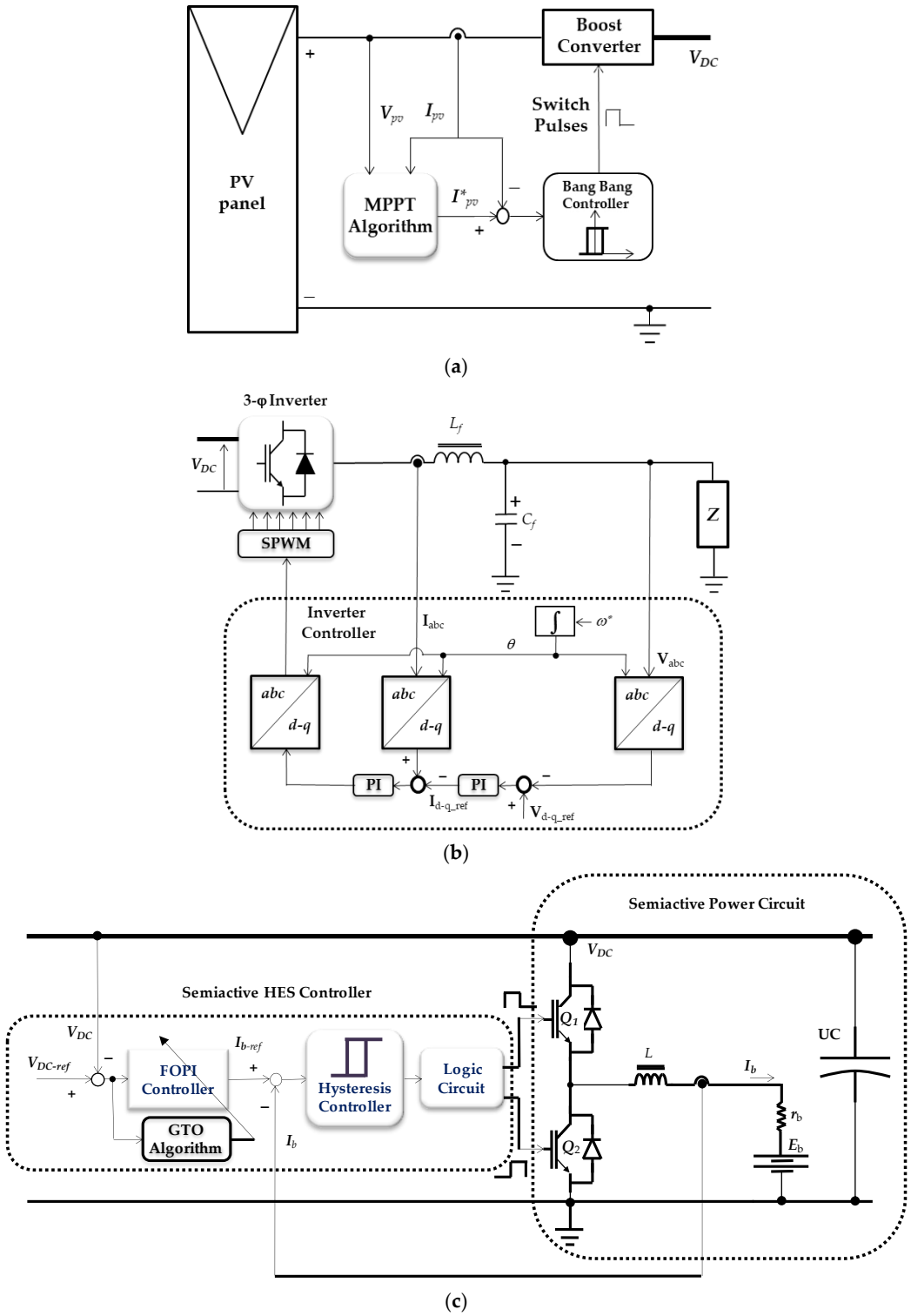

Figure 3. The proposed microgrid's controllers: (**a**) MPPT's regulator, (**b**) output DC/AC's controller, and (**c**) semiactive HESS's controller.

4.2. The Output DC/AC Controller

This controller's goal is to deliver AC power to the load at a controlled frequency and voltage. In Figure 3b, the control loop is displayed. A phase locked loop is used to measure and transmit the load $3-\varphi$ voltages to the d-q frame. The reference values of the transferred d-q voltages are compared with them. A basic PI controller is then fed

the resultant error. Thus, the Ziegler–Nichols method is used to adjust the gains of the PI controller.

4.3. The Semiactive HESS Controller

This controller's primary goal is to control the DC-link voltage, which can be done by managing the semiactive HESS's charging. It has two stacked loops, as Figure 3c illustrates. With the aid of the optimized FOPI controller, the outer loop modifies the DC-link voltage. On the other hand, an additional hysteresis controller assists the inner loop in managing the semiactive HESS charging current. The inner loop's reference charging current is the outer loop's output. The MPPT controllers cease and the controller finishes the charging process when the battery is fully charged.

4.3.1. The FOPI Controller Principles

This regulator's aim is to maintain the DC link voltage (V_{dc}) constant at a predetermined value ($V_{dc\text{-}ref}$). In order to do this, the controller modifies the battery energy storage's charging and discharging procedures. The outer loop of the proposed controller is designed with the help of the FOPI, which preserves the voltage stability of the DC link. Still, the inner loop controls the current drawn from the storage battery. For stability reasons, it has to be made quicker than the outer loop [5].

Any real number can be presented using a complex and flexible integral or differential notation thanks to the controller's use of fractional operators [22]. For a given order q, the following function represents the essential mathematical relationship between the fractional order differential and integral operator:

$$D^{q}_{a,b}f(t) = \begin{cases} f(t) & q = 0 \\ \frac{d^{q}}{dt^{q}}\, f(t) & q > 0 \\ \int_{a}^{b} f(t)d\tau^{-q} & q < 0 \end{cases} \tag{4}$$

where (a, b) indicate the lower and upper limits; if the value of the order q is negative (that is, $q < 0$), it is categorized as a first-order integral; on the other hand, once the value of the order q is positive (that is, $q > 0$), it is categorized as a fractional order differential transfer function.

Because it can be difficult to understand the physical consequences of fractional order, scholars have developed several formulations to help make the concept more understandable. Our comprehension of the fundamental ideas of fractional order is aided by one such formulation, the Riemann–Liouville technique, which provides a way to get the function's order derivative [45]:

$$D^{q}_{a,b}f(t) = \frac{1}{\Gamma(k-q)}\left(\frac{d}{dt}\right)^{k}\int_{a}^{b}\frac{f(\tau)}{(t-\tau)^{n-k+1}}d\tau \tag{5}$$

where $k \in \mathrm{K}$, $q - 1 < q < k$, and the Gamma function $\Gamma(x)$ is defined as,

$$\Gamma(x) = \int_{0}^{\infty} t^{x-1}e^{-t}dt \tag{6}$$

The solution to Equation (7) can be obtained by applying the Laplace transformation to the fractional derivative of R-L in Equation (5) [22]. Equation (8) [46] represents the time domain representation of the n order of the function $f(t)$, and it is derived from Caputo's definition, which is a second definition associated with the idea of fractional order.

$$\mathcal{L}\left\{D^{q}_{0}f(t)\right\} = s^{q}F(s) - \sum_{z=0}^{k-1} s^{z}\left(D^{q-z-1}_{0}f(t)\right)|_{t=0} \tag{7}$$

$$D_{a,b}^{q} f(t) = \begin{cases} \frac{1}{\Gamma(k-q)} \left(\int_a^b \frac{f^k(\tau)}{(t-\tau)^{1-k+q}} d\tau \right) & k-1 < q < k \\ \left(\frac{d}{dt}\right)^k f(t) & q = k \end{cases} \tag{8}$$

An initial condition is associated with the integral order of Equation (14) when the Laplace transformation is performed on it. Equation (9), where s is the Laplace operator, provides an explanation of this beginning condition, which has important physical implications.

$$\mathcal{L}\left\{ D_0^q f(t) \right\} = s^q F(s) - \sum_{z=0}^{k-1} s^{q-z-1} f^{(z)}(0) \tag{9}$$

Completing intricate mathematical computations is required when using the FO operators in the time domain. We frequently employ the recursive approximation method to implement FO operators [47]. An alternative mathematical formula, the Laplace transformation of the qth derivative, can be used to represent it in the following manner:

$$s^q \approx \omega_h^q \prod_{y=-K}^{K} \frac{s + \omega_y'}{s + \omega_y} \tag{10}$$

where

$$\omega_y' = \omega_b \left(\frac{\omega_h}{\omega_b} \right)^{\frac{y+K+(1-q)/2}{2K+1}},$$
$$\omega_y = \omega_b \left(\frac{\omega_h}{\omega_b} \right)^{\frac{y+K+(1+q)/2}{2K+1}},$$

$[\omega_b, \omega_h]$ is the working frequency band and (K) is the approximation order. These parameters have the values: $\omega_b = -1000$, $\omega_h = 1000$, and $K = 5$, in utilizing the Oustaloup algorithm.

The FO proportional integral regulator, which has three tuning gains—proportional gain (A_p), integral gain (A_i), and integral fractional order λ—is used in this investigation. Compared to traditional PI regulators, controllers built with these specific characteristics have been found to provide improved transient time, overall precision, and stability [45]. Additionally, this controller can successfully handle a variety of disturbances due to its increased robustness and adaptability in the face of system interruptions. Additionally, Equation (11) gives the general expression for the FOPI's transfer function in Laplace form, which is represented as $H(s)$, where λ is often between 0 and 1.

$$H(s) = A_p + \frac{A_i}{s^\lambda} \tag{11}$$

A predetermined reference voltage is used to compare the voltage across the DC link to be monitored. The desired battery current reference value is produced by the FOPI controller, which is in charge of controlling the voltage differential. This reference value aids in ensuring that the DC link voltage is properly managed and controlled. As a result, the reference-determined required storage battery current is compared to the actual battery current. This comparison is used by the FOPI controller to calculate and adjust the bidirectional DC/DC converter's duty cycle. Protection is provided by the dual loop controller, which makes sure that the current withdrawn from the battery stays at an acceptable level.

4.3.2. GTO Optimization of the FOPI Parameters

It might be difficult to determine the FOPI gains through trial and error, and it heavily depends on the practitioner's experience and expertise. The task of determining appropriate values for the proposed FOPI parameters might be extremely difficult. It is crucial to meticulously execute this procedure in order to improve the system's functionality and guarantee its stability, hence averting any disturbances. The best values for the FOPI controller's parameter values are found using the metaheuristic optimization technique known as gorilla troop optimization (GTO) [48].

Nowadays, an optimization technique that finds inspiration in the actions of gorilla troops has seen a recent spike in popularity. It is thought to be a brand-new meta-heuristic optimization strategy [49]. The advantages of the GTO optimization over popular optimization methods like PSO or the genetic algorithm (GA) are summarized at Table 1 [50].

Table 1. Summary of the advantages of the GTO optimization versus popular optimization methods.

Issue	GTO Optimization	Popular Optimization Methods	Comments
Premature Convergence	Reduced	Common problem	Due to the exploration–exploitation balance of the GTO.
Handling Nonlinearities	Better	Additional operators like mutation (in GA) are required	
Escape from Local Optima	Better	Common problem	The dynamic encirclement and competition strategies in GTO help it to avoid being trapped in local minima.
Scalability	Handles high-dimensional problems effectively	Less effective	Due to its hierarchical behaviors enabling robust performance with complex problems.
Parameter Tuning	Fewer parameters with less sensitivity to them	More parameters with high sensitivity to them	

Actually, the GTO algorithm's primary source of inspiration is the innate social intelligence of gorilla troops. The gorilla's natural behavior can be summed up in five strategies. The GTO optimizer uses three of them during the exploration stage. These include relocating to the other gorilla, migrating to locations that are known, and migrating to locations that are unknown. The following formulae serve as mathematical models for each of these tactics [51]:

$$GX(i+1) = \begin{cases} min_b + (max_b - min_b) \times r_1 & r_2 < p \\ H \times L + X_{ran}(i)(r_3 - C) & r_2 \geq 0.5 \\ X(i) - L^2 \times (X(i) - GX(i)) + r_4 \times (X(i) - GX_{ran}(i))) & rand < 0.5 \end{cases} \quad (12)$$

$$C = (1 - i/i_{max}) \times F \quad (13)$$

$$F = 1 + cos(2r_5) \quad (14)$$

$$L = l \times C \quad (15)$$

$$H = Z \times X(i), \quad Z = [-C, C] \quad (16)$$

where (min_b, max_b) are the variable limits, $(GX(i+1),\ X(i))$ are the position vectors of the gorilla at two successive iterations, and $(r_6, r_5,\ r_4, r_3, r_2,\ r_1)$ are random positive numbers between [0, 1] produced with a uniform distribution. The parameter (p), which falls within the range [0, 1], specifies the probability of choosing the migration option. When the exploration phase is over, the solution $GX(i)$ will take the place of $X(i)$, and if $GX(i)$'s fitness function value is less than $X(i)$, it will emerge as the silverback. Conversely, the exploitation phase of the GTO optimization process employs strategies like competing for adult females and trailing the silverback. These strategies can be expressed mathematically using Equation (17) through (20). The flow chart that shows the GTO optimization execution steps is shown in Figure 4a.

$$GX(i+1) = X(i) - M \times L \times (X(i) - X_{sb}) + r_4 \times (X(i) - GX_{ran}(i)) \quad (17)$$

$$M = \left(\left| {}^{1}/_{\mathrm{GN}} \sum_{k=1}^{GN} GX_k(i) \right|^{2^L} \right)^{2^{-L}} \tag{18}$$

$$GX(i) = X_{sb} - (Q \times X_{sb} - X(i) \times Q) \times A \tag{19}$$

$$A = \beta \times E, \quad Q = 2r_6 - 1, \quad E = \begin{cases} N_1 & rand \geq 0.5 \\ N_2 & rand < 0.5 \end{cases} \tag{20}$$

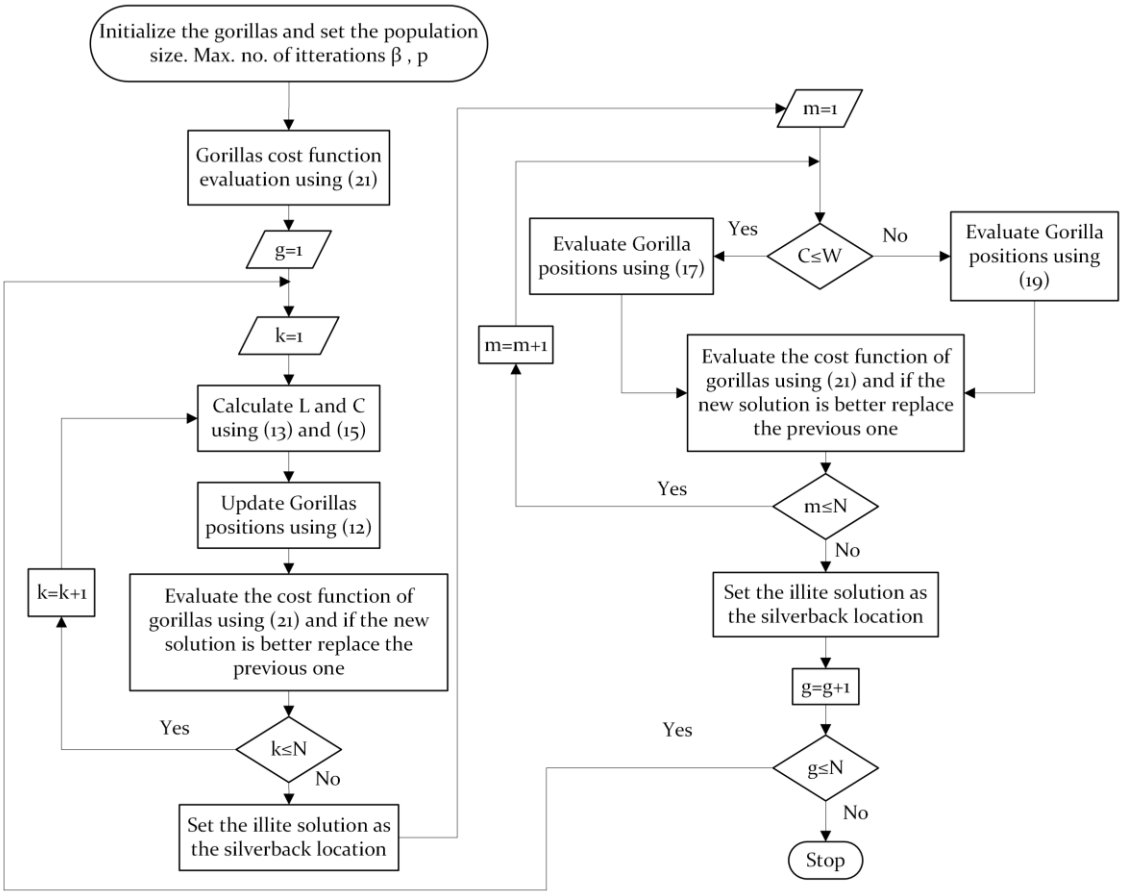

(**a**)

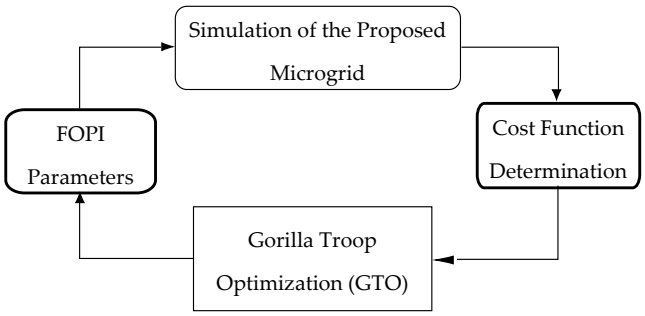

(**b**)

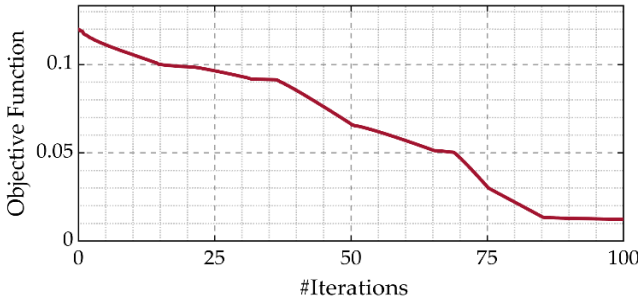

(**c**)

Figure 4. (**a**) The GTO procedure flowchart; (**b**) the optimized FOPI parameters procedure for the semiactive HESS; (**c**) the convergence curve of the GTO used to optimize the FOPI parameters.

When the exploitation stage comes to its end, the cost of $GX(i)$ is compared to that of its corresponding item, $X(i)$. If $GX(i)$ is less expensive than $X(i)$, then $GX(i)$ takes its place and emerges as the optimum choice (silverback).

4.3.3. Determination of the Objective Function

Figure 4b shows the optimized FOPI gain tuning procedure for the semiactive HESS controller's outer loop. The GTO procedure to determine the ideal parameters of the proposed FOPI is summed up in the following points:

1. Establish the gorilla population, which is thought to be a potential answer for the FOPI gains (i.e., three quantities).
2. Using the parameters produced by GTO, simulate the proposed microgrid.
3. To measure the effectiveness of the control system, compute the cost function using the integral square error (ISE).
4. Combine the best answers from the previous phase to create new ones. Determine whether the new solutions are fit.
5. Based on fitness, choose the population's finest solutions.
6. Continue the procedure until the required end points are met.

The GTO's associated parameters are $\beta = 3$, $w = 0.8$, and $p = 0.03$. Equation (21), where T_S is the simulation time, uses the ISE as the objective function for the GTO. Figure 4c displays the convergence curve of the applied GTO, and the optimized FOPI parameters are $K_p = 20$, $K_i = 50$, and $\lambda = 0.05$. The proposed GTO technique is able to achieve a very low objective function estimate of approximately 0.012. Moreover, it is noteworthy that the GTO procedure, taking into account the goal function (ϵ), can approach the optimal gains in a rather short amount of time, usually within 85 iterations.

$$\epsilon = \int_0^{T_S} \left(V_{dc} - V_{dc-ref} \right)^2 dt \tag{21}$$

5. Simulation Findings and Discussions

To verify the paper's theory, the proposed wind/photovoltaic microgrid, shown in Figure 1, is simulated on the MATLAB/Simulink platform. The general specifications of the operating microgrid are displayed in Table 2.

Table 2. The proposed microgrid's specifications.

System Element	Variable	Value
Wind Turbine	Wind speed Power	3.5–25 m/s 10 KW
HESS (Battery/UC)	I_b, V_b UC	800 Ah, 300 V 2 F
AC Bus	Voltage, frequency	220 V, 50 Hz
DC Bus	Voltage	500 V
PV	MPPT I_{sc}, V_{oc}	5440 W 22.8 A, 316.5 V

On testing the system performance during all states, the microgrid is subjected to three types of disturbances. They are the wind speed variations, the variations in the solar irradiation, and the load power changes as presented in Figure 5a, Figure 5b, and Figure 5c respectively. In Figure 5a, the wind speed has speed step changes of 12 m/s, 6.5 m/s, 14 m/s, 0 m/s, and 8 m/s at the instants 0, 0.29 s, 0.62 s, 1 s, and 1.3 s, respectively. However, in Figure 5b, the solar irradiation has step variations of 1 kW/m^2, 0, and 0.5 kW/m^2 at the instants 0, 1 s, and 1.5 s, respectively. On the other hand, the AC load varies in Figure 5c with step changes between 100% full load and 50% full load at the instants 0, 0.42, 0.72 s,

1.38 s, and 1.7 s. The DC bus voltage responses for the GTO-optimized FOPI and PI controllers for the proposed microgrid are shown in Figure 5d. For both controllers, it tracks well with the reference voltage of 500 V. Nevertheless, the GTO-optimized FOPI responds very well. Its settling times are very short and very low maximum overshoot, 0.2%, compared to the PI controller. The PI controller has 3.6% maximum overshoot and 150 ms as a peak settling time.

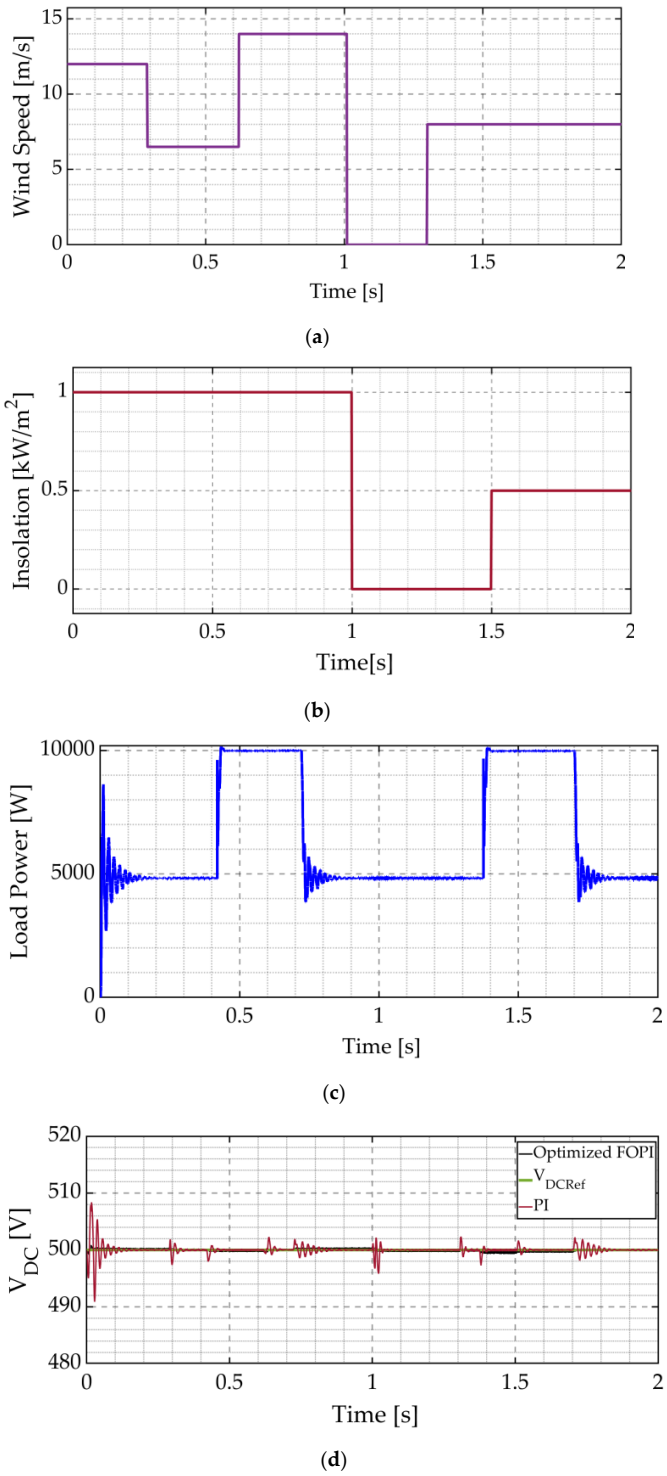

Figure 5. The simulation findings of the proposed microgrid. (**a**) Disturbance in the wind speed, (**b**) disturbance in solar irradiation, (**c**) disturbance in the load power, and (**d**) assessment of the DC link voltage for both controllers without the UC.

Two states are distinguished from the results. In the first state, the optimized FOPI and traditional PI controllers are used to examine the performance of the proposed microgrid without the UC. On the other hand, the second state uses the optimized FOPI controller to demonstrate how the proposed microgrid with a full HESS UC performs. These states are explained in the following paragraphs.

5.1. Performance of the Proposed Microgrid Without UC Using Both Controllers

Figure 6 shows the response of the investigated microgrid, without UC, using the proposed GOT optimized FOPI controller in contrast to the conventional PI controller. Figure 6a,b present the $3-\varphi$ load currents using both controllers and the currents are balanced $3-\varphi$ with stable frequency. The $3-\varphi$ load voltages for each controller are displayed in Figure 6c,d. Despite all of the disruptions, the voltage remains constant in amplitude and maintains a sinusoidal pattern with a consistent frequency. Nevertheless, some transients have occurred at the instants of load changes. The reason behind this effect is the inverter's filter characteristics.

The battery charging and discharging currents using the traditional PI controller are displayed in Figure 6e. Since the PV generation is full and the wind generation is relatively high, corresponding to a wind speed of 12 m/s, the charging current for the interval of 0 to 0.3 s is 17 A, that is, comparatively high. As the PV power reaches its peak and the wind power decreases, the charging current for the duration 0.3 to 0.42 s is 5 A, which is reasonable. At the instant 0.42 s, the load is increased to full load. Consequently, the battery discharges to balance for the required demand. When both the PV power and the wind power are fully utilized, at the period 0.62 s to 1 s, which corresponds to a wind speed of 14 m/s, the charging current is 21 A. As the load increases, the charging current decreases during all periods. Both wind and photovoltaic energy are suppressed for 1 s–1.3 s. Because of this, the storage battery will make up for them throughout this time, with a discharging current of 18 A. The same rules are applied during the remaining time of operation. Additionally, Figure 6f shows the current response of the battery for the proposed controller. It successfully tracks its reference for each controller. The DC bus voltage controller generates the reference value for the battery's current. The charging and discharging operations account for radiation variations in addition to tracking their references. Figure 6g,h display the battery's SOC performance for both the conventional PI controllers and the proposed FOPI controllers. The SOC's response for each of the two regulators is almost the same. The steps for charging and discharging are presented, nevertheless. The load current spectrum analysis using the proposed FOPI and PI controllers is displayed in Figure 6i,j. For the proposed FOPI controller, the load current THD is 0.42%. But in the case of the PI controller, it is 0.72%. In all scenarios, the load current THD is less than the requirements stated in standards [52]. As a result, the proposed FOPI controller has a higher load current quality than the PI controller.

5.2. Performance of the Proposed Microgrid with UC Using the Optimized FOPI Controller

Figure 7 shows the response of the investigated microgrid (with UC) using the proposed GOT optimized FOPI controller. Hence, the semiactive HESS acts effectively in this case. The response of the DC-link voltage including the proposed regulator is presented in Figure 7a. It seems ideal as there are no transients corresponding to all kinds of disturbances from the solar irradiation, wind speed, and load variations as provided by Figure 5. Compared to the response without the UC, in Figure 5d, there are no transients at all with the presence of a UC. However, it can be concluded that the proposed GOT optimized FOPI controller can provide nearly the same performance as that with the UC. Hence, the proposed controller can reduce the cost, weight, and space of the system. The UC current waveform is present in Figure 7b. It has a high frequency pattern to compensate for the transients in the DC-link voltage variations. Also, the current oscillates around zero to indicate the stability of the DC-link voltage at steady state.

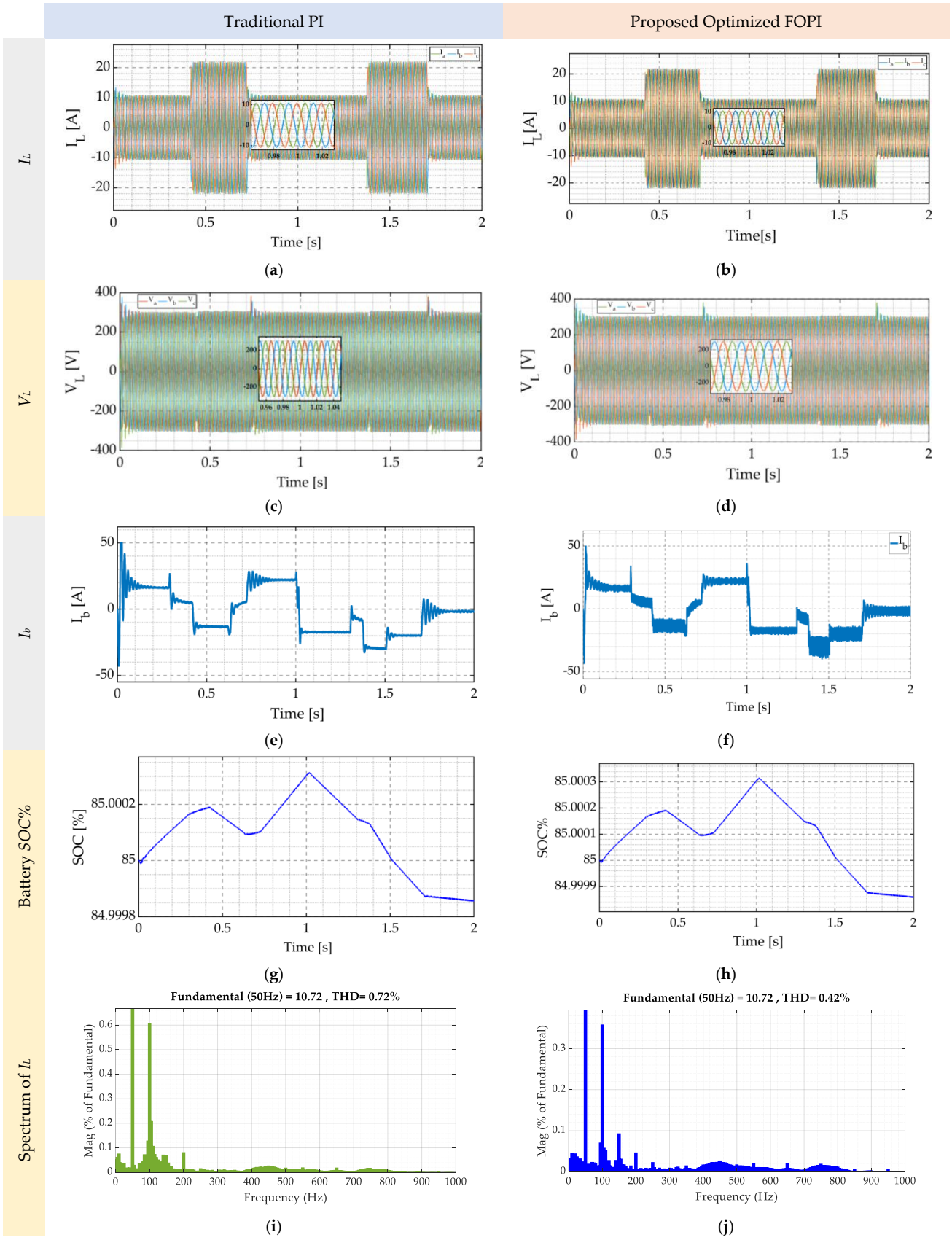

Figure 6. The response of the investigated microgrid (without UC) using the traditional PI controller (**a**,**c**,**e**,**g**,**i**) in comparison to the proposed GOT optimized FOPI controller (**b**,**d**,**f**,**h**,**j**).

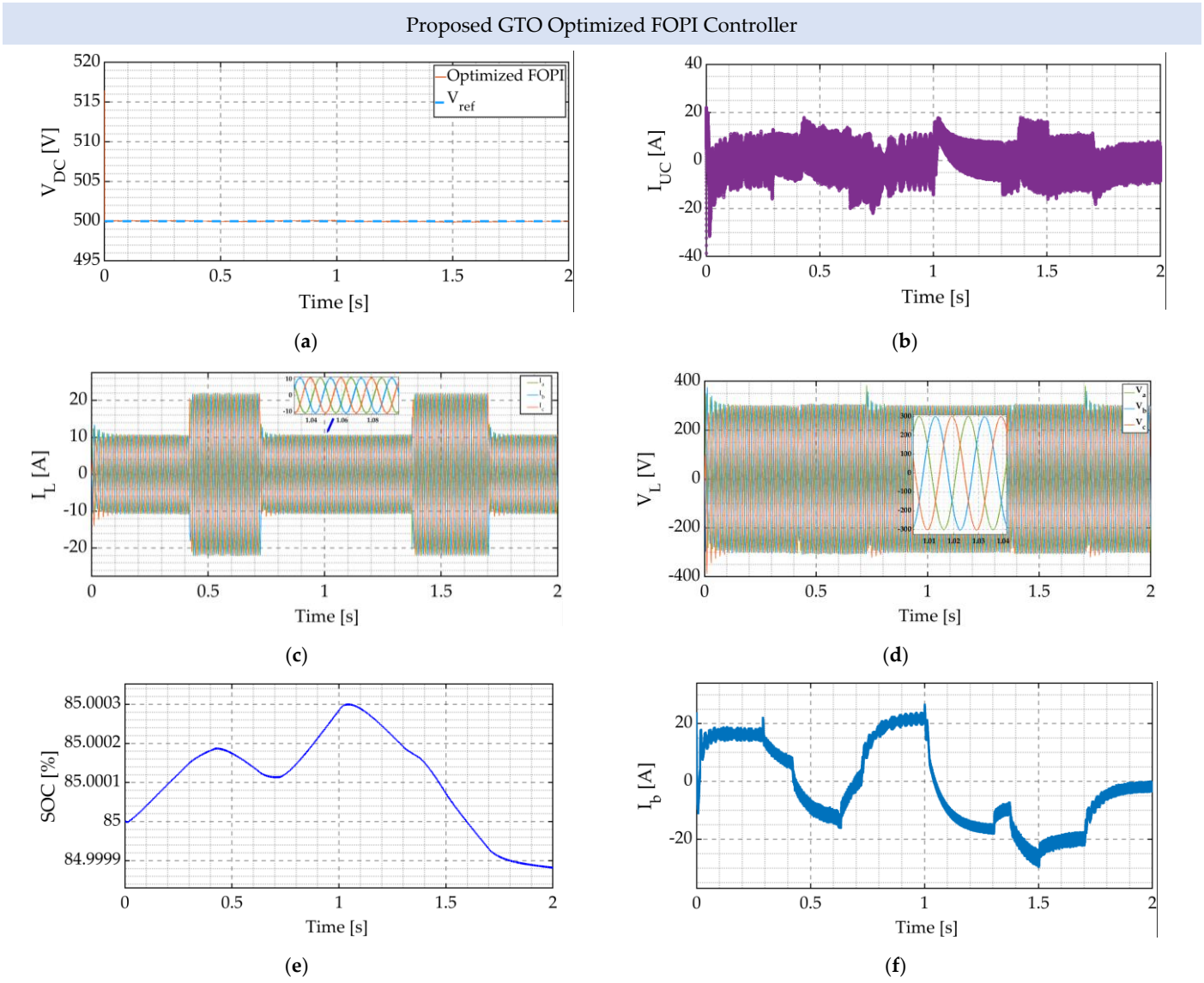

Figure 7. The response of the investigated microgrid (with the UC) using the proposed GOT optimized FOPI controller (**a**–**f**).

In Figure 7c,d, the load voltage and current are displayed. Despite all of the disruptions, the voltage remains constant in amplitude and maintains a sinusoidal pattern with a consistent frequency. The battery SOC response is presented in Figure 7e. It seems to have the same character as the case without the UC, displayed in Figure 6h. Figure 7f displays the battery current response with the proposed GTO optimized FOPI controller. Except for the high-frequency waves uploaded on the battery current, the response is resampling to that without the UC.

Figure 8 shows the power response of the wind, PV, battery, and UC for the proposed GTO optimized FOPI controller. Figure 8a displays the wind turbine power during the operating time. It is noted that wind power tracks its MPPT conditions well. Also, the PV power response follows its MPPT conditions well, as displayed in Figure 8b. Those reflect the perfect operation of the MPPT subsystems for both the wind and PV supplies. Figure 8c presents the battery power performance. When the battery power is positive, it indicates battery charging. On the other hand, when it is negative, the battery is discharging. For example, in the period 0.42 s to 0.72 s, the battery discharges due to the low generated wind energy and high demand full load. Also, for the time after 1 s, the battery discharges as the

generated wind and PV energies are low and the demand fluctuates between 50% to 100% full load.

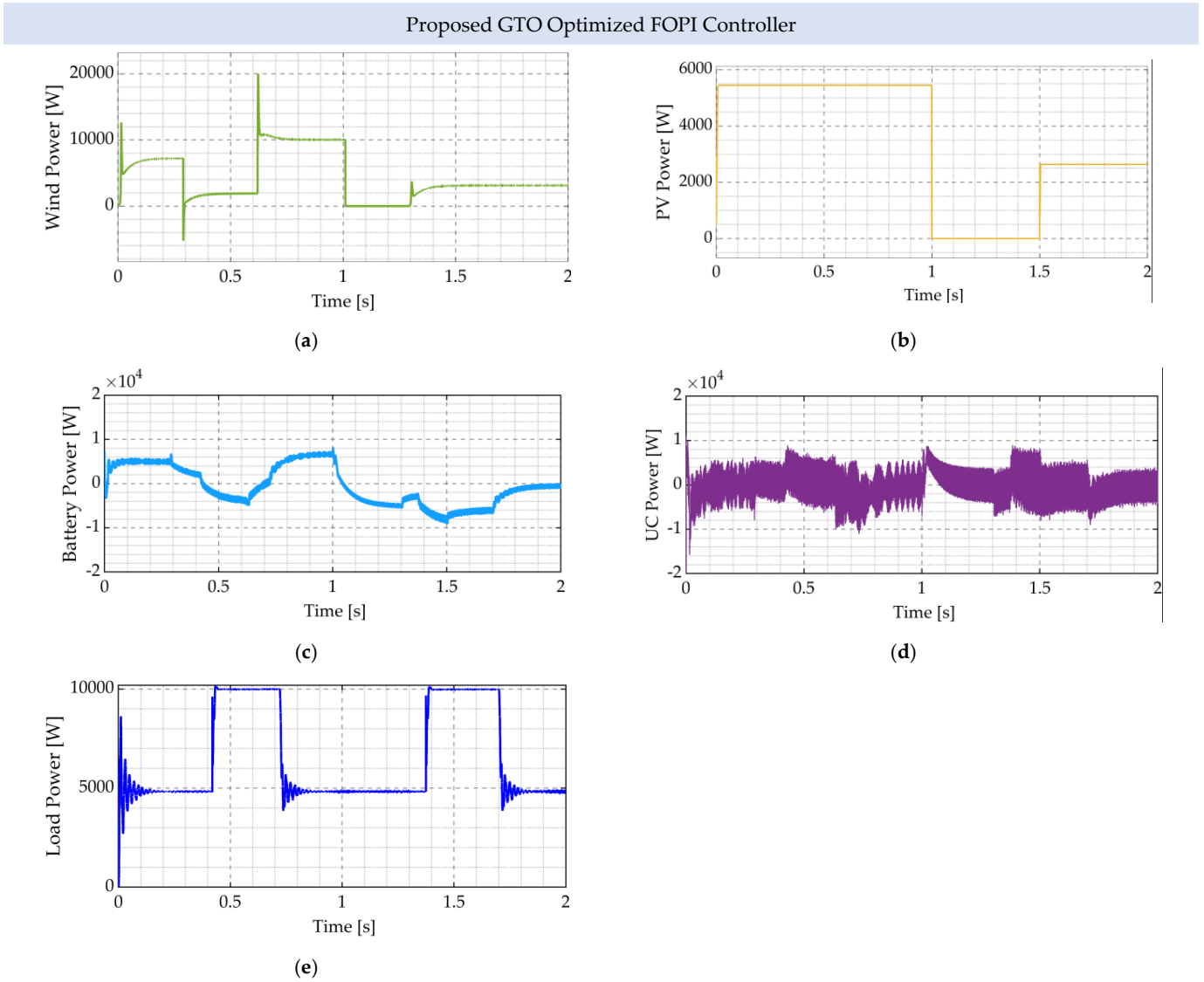

Figure 8. The power performance of the investigated microgrid (with the UC) using the proposed GOT optimized FOPI controller (**a**–**e**).

Figure 8d indicates the UC power response. It has high frequency transients as it is expected to be a sink for voltage transients. The load power is presented in Figure 8e. There are some transient oscillations at the step instants due to the electrical characteristics of the output filter of the load inverter. Also, it must be noted that the rated power of the PV is 5.44 KW, which is ≈50% of the full load. Hence, the PV cannot supply the full load without any support from the battery or the wind energy. Refer to Figure 8 and track the power for the time range 0.42 s to 0.5 s, where the load became 10 KW. It is found that the sum of the PV and the wind power is less than the load demand. Therefore, the battery power reverses its direction to support the drop in energy. By the same way, the power balance of the system can be checked, and also the energy management and control can be proven.

The assessment of the maximum overshoot for each period of the results utilizing the standard PI controller and the proposed FOPI is presented in Table 3. For a variety of types of disturbances in the load power (P_l), wind speed (ω_S), and solar insulation (I_n), the peak overshoot of V_{DC} using the proposed FOPI is much smaller than that using the conventional PI controller.

Table 3. Maximum DC link voltage overshoot using both the traditional PI controller and the proposed optimized FOPI.

Time (s)	Disturbance (%)	Peak Overshoot of V_{DC} (%)		Settling Time (s)	
		GTO Optimized FOPI	Traditional PI	GTO Optimized FOPI	Traditional PI
0	$\Delta\omega_S = 86\%$, $\Delta P_l = 50\%$, $\Delta I_n = 100\%$	0.2%	3.6%	0.04	0.2
0.29	$\Delta\omega_S = -46\%$	~0.01	0.9%	~0.0	0.08
0.42	$\Delta P_l = 50\%$	~0.01	0.6%	~0.0	0.06
0.62	$\Delta\omega_S = 46\%$	~0.01	0.6%	~0.0	0.07
0.72	$\Delta P_l = -50\%$	~0.01	0.7%	~0.0	0.16
1	$\Delta\omega_S = -100\%$, $\Delta I_n = -100\%$	~0.01	1%	~0.0	0.07
1.3	$\Delta\omega_S = 57\%$	~0.01	0.6%	~0.0	0.065
1.38	$\Delta P_l = 50\%$	~0.01	0.6%	~0.0	0.055
1.5	$\Delta I_n = +50\%$	~0.01	0.4%	~0.0	0.06
1.7	$\Delta P_l = -50\%$	~0.01	0.8%	~0.0	0.15

5.3. HIL Validation Results

To evaluate the proposed system and validate the simulation results, a Hardware-in-the-Loop (HIL) emulator was implemented using a C2000™ microcontroller LaunchPad™ TMS320F28379D kit, (Texas Instruments, Dallas, TX, USA) as presented in Figure 9. In this setup, the HIL emulator partitions the system, typically hosting the power components as a model in MATLAB on a personal computer. The power units of the proposed system, including the photovoltaic (PV) arrays, wind turbines, power converters, battery, supercapacitor, and filters, are simulated within MATLAB. Meanwhile, the control algorithms—specifically the FOPI—are executed on the microcontroller kit. Communication between the PC and the microcontroller is established via a virtual serial COM port [53–55], allowing MATLAB to send measured power circuit signals, such as the DC bus voltage, to the microcontroller. The microcontroller then processes the control algorithms and generates the switching signals for the power converter. Data exchange between the PC and the microcontroller is synchronized at each sampling interval.

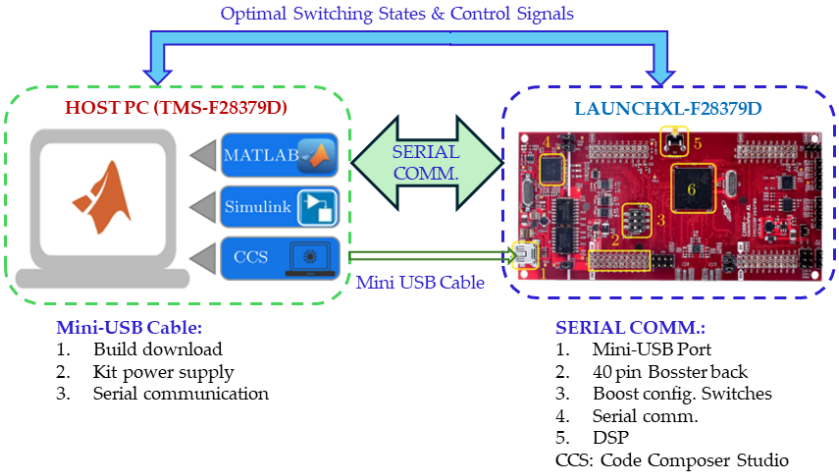

Figure 9. Schematic diagram of the HIL simulation based on the DSP target LaunchPadXLTMS320F28379D kit.

Figure 10 presents the response of the investigated microgrid (with the UC) using the GTO optimized FOPI controller utilizing the HIL with the DSP target LaunchPadXLTMS320F28379D kit (Texas Instruments, Dallas, TX, USA). The results are fairly close to those shown in Figure 7.

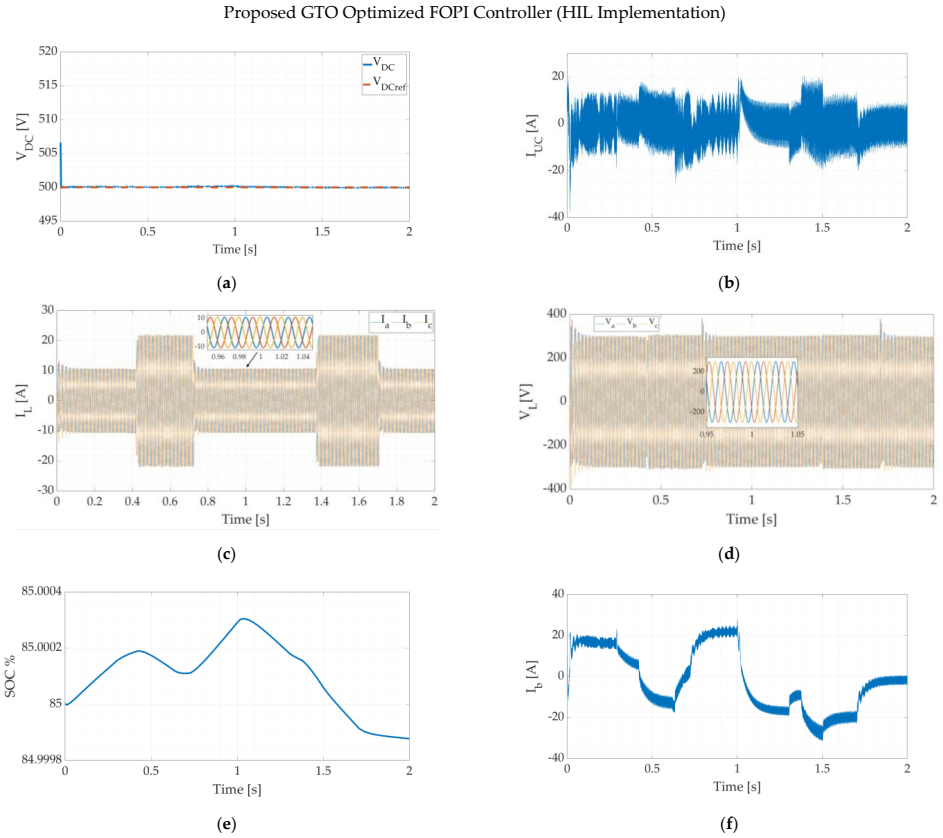

Figure 10. The response of the investigated microgrid (with the UC) using the proposed FOPI controller utilizing the HIL with a DSP target LaunchPadXLTMS320F28379D kit (**a**–**f**).

6. Conclusions

A hybrid wind/photovoltaic microgrid that operates in standalone mode and makes use of hybrid storage (ultracapacitor/battery) is proposed. The latest fractional-order PI (FOPI) control approach serves as the foundation for the microgrid's energy management and control. A wind turbine, photovoltaic array, two step up DC/DC converters, semiactive HESS system, two-way DC/DC converter, and DC/AC load inverter are all part of the microgrid. The P&O procedure was employed to obtain the MPPT conditions for the PV and the wind turbine. The proposed control scheme for the semiactive HESS consists of double loops: an inner loop that uses the hysteresis controller to regulate the battery current and an outer loop that uses a FOPI controller to control the DC-link voltage. To attain optimal performance, the gorilla troop optimization (GTO) approach was utilized to improve the parameters of the FOPI.

MATLAB was used to simulate the proposed microgrid with the optimized FOPI controller. According to the simulation results, the classical PI controller's system responses are inferior to those of the GTO optimized FOPI controller. Different wind speeds, sun insolation levels, and load powers were used to evaluate the system. The load voltage was sinusoidal with perfect responsiveness, maintaining a constant frequency and amplitude for all disturbances. For the proposed controller, the maximum overshoot can reach a maximum value of 0.2%. In the case of the PI controller, it is 3.6%. It was also found that in the presence of the UC, the microgrid performance was improved. However, the improvement was very close to that gained when using the proposed controller without the UC. Hence, the proposed controller can reduce the cost, weight, and space of the system.

This reduction has important ramifications for creating distributed energy systems that are hybrids and will facilitate the global integration of renewable energy resources. Future research might concentrate on improving the recently developed intelligent fractional order controllers for the microgrid's independent and grid-connected modes. Also, the

demand management via distributed control and human-in-the-loop optimization could be applied to a wind/PV microgrid-connected system as in [56]. Finally, a HIL emulator was implemented using a C2000™ microcontroller LaunchPad™ TMS320F28379D kit to evaluate the proposed system and validate the simulation findings.

Author Contributions: S.A.Z. and H.A. handled the formal analysis and conceptualization; H.A. assessed and re-reviewed the article; and A.M.A. and M.A.M. helped with funding acquisition. All authors have read and agreed to the published version of the manuscript.

Funding: This research was funded by the Deputyship for Research and Innovation, Ministry of Education, Saudi Arabia through the University of Tabuk, grant number S-1444-0070.

Data Availability Statement: Data is contained within the article.

Acknowledgments: The authors extend their appreciation to the Deanship of Research and Graduate Studies at University of Tabuk for funding this work through Research number S-1444-0070.

Conflicts of Interest: The authors declare no conflicts of interest.

Nomenclature

PV	photovoltaic
UC	ultra-capacitor
PID	proportional integral derivative
FOPI	fractional-order proportional integral
FOC	fractional-order control
FO	fractional order
DC	direct current
AC	alternating current
PWM	pulse width modulation
MPPT	maximum power point tracking
HESS	hybrid energy storage system
HES	high energy storage
HPS	high power storage
P_g, P_s, and P_l	power produced, power transferred by HESS, and power used by the load
P_{HPS}, P_{HES}	power supplied by the HPS and HES elements
μ and α	controllability representing variables
SMES	super conducting magnetic energy storage
$V_{dc\text{-}ref}$, V_{dc}	DC link reference voltage and its actual value
(a, b)	lower and upper limits
q	order of differentiation
ω_b, ω_h	working frequency band
K	approximation order
(A_p, A_i)	proportional gain, integral gain
H(s)	FOPI's transfer function
(min_b, max_b)	variable limits
$GX(i+1)$, $GX(i)$	position vectors of the gorilla at two successive iterations
$r_6, r_5, r_4, r_3, r_2, r_1$	random positive numbers between [0, 1] produced with a uniform distribution
β, w, and p	GTO's weighting parameters
GTO	gorilla troop optimization
ISE	integral square error
ϵ	cost function
I_{SC}, V_{OC}	PV short circuit current, open circuit voltage
V_b, I_b	battery voltage and current
ω_S	wind speed
I_n	solar insulation
PSO	particle swarm optimization
GA	genetic algorithms
SOC	state of charge

References

1. Bhimaraju, A.; Mahesh, A. Recent developments in PV/wind hybrid renewable energy systems: A review. *Energy Syst.* **2024**, *15*. [CrossRef]
2. Kartal, M.T.; Pata, U.K.; Alola, A.A. Renewable electricity generation and carbon emissions in leading European countries: Daily-based disaggregate evidence by nonlinear approaches. *Energy Strat. Rev.* **2024**, *51*, 101300. [CrossRef]
3. Meng, D.; Yang, S.; Yang, H.; De Jesus, A.M.; Correia, J.; Zhu, S.P. Intelligent-inspired framework for fatigue reliability evaluation of offshore wind turbine support structures under hybrid uncertainty. *Ocean Eng.* **2024**, *307*, 118213. [CrossRef]
4. Peters, R.; Berlekamp, J.; Kabiri, C.; Kaplin, B.A.; Tockner, K.; Zarfl, C. Sustainable pathways towards universal renewable electricity access in Africa. *Nat. Rev. Earth Environ.* **2024**, *5*, 137–151. [CrossRef]
5. Albalawi, H.; El-Shimy, M.E.; AbdelMeguid, H.; Kassem, A.M.; Zaid, S.A. Analysis of a Hybrid Wind/Photovoltaic Energy System Controlled by Brain Emotional Learning-Based Intelligent Controller. *Sustainability* **2022**, *14*, 4775. [CrossRef]
6. Albalawi, H.; Kassem, A.M.; Zaid, S.A.; Lakhouit, A.; Arshad, M.A. Energy management of an isolated wind/photovoltaic microgrid using cuckoo search algorithm. *Intell. Autom. Soft Comput.* **2022**, *34*, 2051–2066. [CrossRef]
7. Hybrid Wind and Solar Electric Systems.(22C.E.). Available online: https://www.energy.gov/energysaver/hybrid-wind-and-solar-electric-systems (accessed on 1 August 2024).
8. Angadi, S.; Yaragatti, U.R.; Suresh, Y.; Raju, A.B. Comprehensive review on solar, wind and hybrid wind-PV water pumping systems-an electrical engineering perspective. *CPSS Trans. Power Electron. Appl.* **2021**, *6*, 1–19. [CrossRef]
9. Pradhan, S.; Singh, B.; Panigrahi, B.K.; Murshid, S. A composite sliding mode controller for wind power extraction in remotely located solar PV–wind hybrid system. *IEEE Trans. Ind. Electron.* **2019**, *66*, 5321–5331. [CrossRef]
10. Setiawan, B.; Putra, E.S.; Siradjuddin, I.; Junus, M. Optimisation solar and wind hybrid energy formod elcatamaran ship. *IOP Conf. Ser. Mater. Sci. Eng.* **2021**, *1073*, 012044. [CrossRef]
11. Bouchekara, H.R.E.H.; Sha'aban, Y.A.; Shahriar, M.S.; Abdullah, S.M.; Ramli, M.A. Sizing of Hybrid PV/Battery/Wind/Diesel Microgrid System Using an Improved Decomposition Multi-Objective Evolutionary Algorithm Considering Uncertainties and Battery Degradation. *Sustainability* **2023**, *15*, 11073. [CrossRef]
12. Liu, J.; Cao, S.; Chen, X.; Yang, H.; Peng, J. Energy planning of renewable applications in high-rise residential buildings integrating battery and hydrogen vehicle storage. *Appl. Energy* **2021**, *281*, 116038. [CrossRef]
13. Rezkallah, M.; Hamadi, A.; Chandra, A.; Singh, B. Design and implementation of active power control with improved P&O method for wind-PV-battery-based standalone generation system. *IEEE Trans. Ind. Electron.* **2018**, *65*, 5590–5600.
14. Parida, A.; Chatterjee, D. Stand-alone AC-DC microgrid-based wind solar hybrid generation scheme with autonomous energy exchange topologies suitable for remote rural area power supply. *Int. Trans. Electr. Energy Syst.* **2018**, *28*, 2520. [CrossRef]
15. Jamshidi, S.; Pourhossein, K.; Asadi, M. Size estimation of wind/solar hybrid renewable energy systems without detailed wind and irradiation data: A feasibility study. *Energy Convers. Manag.* **2021**, *234*, 113905. [CrossRef]
16. Zaid, S.A.; Kassem, A.M.; Alatwi, A.M.; Albalawi, H.; AbdelMeguid, H.; Elemary, A. Optimal Control of an Autonomous Microgrid Integrated with Super Magnetic Energy Storage Using an Artificial Bee Colony Algorithm. *Sustainability* **2023**, *15*, 8827. [CrossRef]
17. Muresan, C.I.; Birs, I.; Ionescu, C.; Dulf, E.H.; De Keyser, R. A Review of Recent Developments in Autotuning Methods for Fractional-Order Controllers. *Fractal Fract.* **2022**, *6*, 37. [CrossRef]
18. Monje, C.A.; Chen, Y.Q.; Vinagre, B.M.; Xue, D.; Feliu, V. *Fractional-Order Systems and Controls: Fundamentals and Applications*; Springer: Berlin/Heidelberg, Germany, 2010.
19. Da Silva, C.S.M.; Da Silva, N.J.F.; Júnior, F.A.D.C.A.; De Medeiros, R.L.P.; E Silva, L.E.S.; De Lucena, V.F. Experimental Implementation of Hydraulic Turbine Dynamics and a Fractional Order Speed Governor Controller on a Small-Scale Power System. *IEEE Access* **2024**, *12*, 40480–40495. [CrossRef]
20. Zaheeruddin; Singh, K. Load frequency regulation by de-loaded tidal turbine power plant units using fractional fuzzy based PID droop controller. *Appl. Soft Comput.* **2020**, *92*, 106338. [CrossRef]
21. Pan, I.; Das, S. Fractional order AGC for distributed energy resources using robust optimization. *IEEE Trans. Smart Grid* **2016**, *7*, 2175–2186. [CrossRef]
22. Zaid, S.A.; Bakeer, A.; Magdy, G.; Albalawi, H.; Kassem, A.M.; El-Shimy, M.E.; AbdelMeguid, H.; Manqarah, B. A New Intelligent Fractional-Order Load Frequency Control for Interconnected Modern Power Systems with Virtual Inertia Control. *Fractal Fract.* **2023**, *7*, 62. [CrossRef]
23. Lazard's Levelized Cost of Energy Analysis—Version 16. Available online: https://www.lazard.com/research-insights/2023-levelized-cost-of-energyplus/ (accessed on 4 April 2023).
24. Soudagar, M.E.M.; Ramesh, S.; Khan, T.Y.; Almakayeel, N.; Ramesh, R.; Ghazali, N.N.N.; Cuce, E.; Shelare, S. An overview of the existing and future state of the art advancement of hybrid energy systems based on PV-solar and wind. *Int. J. Low-Carbon Technol.* **2024**, *19*, 207–216. [CrossRef]
25. Shi, X.; Shi, X.; Dong, W.; Zang, P.; Jia, H.; Wu, J.; Wang, Y. Research on Energy Storage Configuration Method Based on Wind and Solar Volatility. In Proceedings of the 2020 10th International Conference on Power and Energy Systems (ICPES), Chengdu, China, 25–27 December 2020; pp. 464–468. [CrossRef]
26. Ma, T.; Yang, H.; Lu, L. Development of hybrid battery–supercapacitor energy storage for remote area renewable energy systems. *Appl. Energy* **2015**, *153*, 56–62. [CrossRef]

27. Tammineedi, C. *Modeling Battery-Ultracapacitor Hybrid Systems for Solar and Wind Applications*; The Pennsylvania State University: University Park, PA, USA, 2011.
28. Ribeiro, E.; Cardoso, A.J.M.; Boccaletti, C. Power conditioning supercapacitors in combination with batteries for stand-alone power systems. In Proceedings of the 2012 International Symposium on Power Electronics, Electrical Drives, Automation and Motion (SPEEDAM), Sorrento, Italy, 20–22 June 2012; pp. 914–919.
29. Babu, T.S.; Vasudevan, K.R.; Ramachandaramurthy, V.K.; Sani, S.B.; Chemud, S.; Lajim, R.M. A Comprehensive Review of Hybrid Energy Storage Systems: Converter Topologies, Control Strategies and Future Prospects. *IEEE Access* **2020**, *8*, 148702–148721. [CrossRef]
30. Chen, H.; Cong, T.N.; Yang, W.; Tan, C.; Li, Y.; Ding, Y. Progress in electrical energy storage system: A critical review. *Prog. Nat. Sci.* **2009**, *19*, 291–312. [CrossRef]
31. Spataru, C.; Kok, Y.C.; Barrett, M. Physical energy storage employed worldwide. *Energy Procedia* **2014**, *62*, 452–461. [CrossRef]
32. Zhan, Y.; Guo, Y.; Zhu, J.; Li, L. Power and energy management of grid/PEMFC/battery/supercapacitor hybrid power sources for UPS applications. *Int. J. Electr. Power Energy Syst.* **2015**, *67*, 598–612. [CrossRef]
33. Jing, W.; Hung Lai, C.; Wong, S.H.W.; Wong, M.L.D. Battery-supercapacitor hybrid energy storage system in standalone DC microgrids: A review. *IET Renew. Power Gener.* **2017**, *11*, 461–469. [CrossRef]
34. Gu, Y.; Xiang, X.; Li, W.; He, X. Mode-Adaptive Decentralized Control for Renewable DC Microgrid with Enhanced Reliability and Flexibility. *IEEE Trans. Power Electron.* **2014**, *29*, 5072–5508. [CrossRef]
35. Bahrami, S.; Wong, V.W.S.; Jatskevich, J. Optimal power flow for AC-DC networks. In Proceedings of the 2014 IEEE International Conference on Smart Grid Communications (SmartGridComm), Venice, Italy, 3–6 November 2014; pp. 49–54.
36. Che, L.; Shahidehpour, M. DC microgrids: Economic operation and enhancement of resilience by hierarchical control. *IEEE Trans. Smart Grid* **2014**, *5*, 2517–2526.
37. Lahyani, A.; Venet, P.; Guermazi, A.; Troudi, A. Battery/supercapacitors combination in uninterruptible power supply (UPS). *IEEE Trans. Power Electron.* **2013**, *28*, 1509–1522. [CrossRef]
38. Cao, J.; Emadi, A. A new battery/UltraCapacitor hybrid energy storage system for electric, hybrid, and plug-in hybrid electric vehicles. *IEEE Trans. Power Electron.* **2012**, *27*, 122–132.
39. Cohen, I.J.; Wetz, D.A.; Heinzel, J.M.; Dong, Q. Design and characterization of an actively controlled hybrid energy storage module for high-rate directed energy applications. *IEEE Trans. Plasma Sci.* **2015**, *43*, 1427–1433. [CrossRef]
40. Kollimalla, S.K.; Mishra, M.K.; Ukil, A.; Gooi, H.B. DC grid voltage regulation using new HESS control strategy. *IEEE Trans. Sustain. Energy* **2017**, *8*, 772–781. [CrossRef]
41. Manandhar, U.; Tummuru, N.R.; Kollimalla, S.K.; Ukil, A.; Beng, G.H.; Chaudhari, K. Validation of faster joint control strategy for batteryand supercapacitor-based energy storage system. *IEEE Trans. Ind. Electron.* **2018**, *65*, 3286–3295. [CrossRef]
42. Song, Z.; Hofmann, H.; Li, J.; Han, X.; Zhang, X.; Ouyang, M. A comparison study of different semi-active hybrid energy storage system topologies for electric vehicles. *J. Power Sources* **2015**, *274*, 400–411. [CrossRef]
43. Gee, A.M.; Robinson, F.V.P.; Dunn, R.W. Analysis of battery lifetime extension in a small-scale wind-energy system using supercapacitors. *IEEE Trans. Energy Convers.* **2013**, *28*, 24–33. [CrossRef]
44. Bingi, K.; Prusty, R.; Singh, A. A Review on Fractional-Order Modelling and Control of Robotic Manipulators. *Fractal Fract.* **2023**, *7*, 77. [CrossRef]
45. Zaid, S.A.; Bakeer, A.; Albalawi, H.; Alatwi, A.M.; AbdelMeguid, H.; Kassem, A.M. Optimal Fractional-Order Controller for the Voltage Stability of a DC Microgrid Feeding an Electric Vehicle Charging Station. *Fractal Fract.* **2023**, *7*, 677. [CrossRef]
46. Morsali, J.; Zare, K.; Hagh, M.T. Applying fractional order PID to design TCSC-based damping controller in coordination with automatic generation control of interconnected multi-source power system. *Eng. Sci. Technol. Int. J.* **2017**, *20*, 1–17. [CrossRef]
47. Shaheen, A.; Ginidi, A.; El-Sehiemy, R.; Elsayed, A.; Elattar, E.; Dorrah, H.T. Developed Gorilla Troops Technique for Optimal Power Flow Problem in Electrical Power Systems. *Mathematics* **2022**, *10*, 1636. [CrossRef]
48. Ali, M.; Kotb, H.; Aboras, K.M.; Abbasy, N.H. Design of Cascaded PI-Fractional Order PID Controller for Improving the Frequency Response of Hybrid Microgrid System Using Gorilla Troops Optimizer. *IEEE Access* **2021**, *9*, 150715–150732. [CrossRef]
49. El-Dabah, M.A.; Hassan, M.H.; Kamel, S.; Zawbaa, H.M. Robust Parameters Tuning of Different Power System Stabilizers Using a Quantum Artificial Gorilla Troops Optimizer. *IEEE Access* **2022**, *10*, 82560–82579. [CrossRef]
50. Abualigah, L.; Diabat, A.; Mirjalili, S.; Abd Elaziz, M.; Gandomi, A.H. The Arithmetic Optimization Algorithm. *Comput. Methods Appl. Mech. Eng.* **2021**, *376*, 113609. [CrossRef]
51. Saad, S.S.; Zainuri, M.A.A.M.; Hussain, A. Implementation of Maximum Power Point Tracking Techniques for PV-Wind Hybrid Energy System: A Review. In Proceedings of the 2021 International Conference on Electrical Engineering and Informatics (ICEEI), Kuala Terengganu, Malaysia, 12–13 October 2021; pp. 1–6. [CrossRef]
52. *IEEE-519*; IEEE Recommended Practices and Requirements for Harmonic Control in Electric Power Systems. IEEE: New York, NY, USA, 1992.
53. Bakeer, A.; Mohamed, I.S.; Malidarreh, P.B.; Hattabi, I.; Liu, L. An Artificial Neural Network-Based Model Predictive Control for Three-Phase Flying Capacitor Multilevel Inverter. *IEEE Access* **2022**, *10*, 70305–70316. [CrossRef]
54. Zaid, S.A.; Mohamed, I.S.; Bakeer, A.; Liu, L.; Albalawi, H.; Tawfiq, M.E.; Kassem, A.M. From *MPC*-Based to End-to-End *(E2E)* Learning-Based Control Policy for Grid-Tied *3L-NPC* Transformerless Inverter. *IEEE Access* **2022**, *10*, 57309–57326. [CrossRef]

55. Abid, A.; Bakeer, A.; Zellouma, L.; Bouzidi, M.; Lashab, A.; Rabhi, B. Low Computational Burden Predictive Direct Power Control of Quasi Z-Source Inverter for Grid-Tied PV Applications. *Sustainability* **2023**, *15*, 4153. [CrossRef]
56. Korkas, C.D.; Baldi, S.; Kosmatopoulos, E.B. Grid-connected microgrids: Demand management via distributed control and human-in-the-loop optimization. In *Advances in Renewable Energies and Power Technologies*; Elsevier: Amsterdam, The Netherlands, 2018; pp. 315–344.